Anomalous Nernst Effect in an Antiperovskite Antiferromagnet

Yunfeng You,[1] Hei Lam,[2] Caihua Wan,[3] Chunlei Wan,[4] Wenxuan Zhu,[1] Lei Han,[1] Hua Bai,[1] Yongjian Zhou,[1] Leilei Qiao,[1] Tongjin Chen,[1] Feng Pan,[1] Junwei Liu,[2] and Cheng Song[1,*]

[1] *Key Laboratory of Advanced Materials, School of Materials Science and Engineering, Tsinghua University, Beijing 100084, China*

[2] *Department of Physics, Hong Kong University of Science and Technology, Hong Kong 00852, China*

[3] *Beijing National Laboratory for Condensed Matter Physics, Institute of Physics, Chinese Academy of Sciences, Beijing 100190, China*

[4] *State Key Lab of New Ceramics and Fine Processing, School of Materials Science and Engineering, Tsinghua University, Beijing 100084, China*

(Received 17 November 2021; revised 22 June 2022; accepted 19 July 2022; published 2 August 2022)

The anomalous Nernst effect (ANE), the generation of a transverse electric voltage by a longitudinal temperature gradient, has attracted increasing interest from researchers recently, due to its potential in thermoelectric power conversion and close relevance to the Berry curvature of the band structure. Avoiding the stray field of ferromagnets, the ANE in antiferromagnets (AFMs) has the advantage of realizing highly efficient and densely integrated thermopiles. Here, we report the observation of the ANE in an antiperovskite noncollinear AFM, Mn_3SnN, experimentally, which is triggered by the enhanced Berry curvature from Weyl points located close to the Fermi level. Considering that antiperovskite Mn_3SnN has a rich magnetic phase transition, we modulate the noncollinear AFM configurations by the biaxial strain, which enables us to control its ANE. Our findings provide a potential class of materials to explore the Weyl physics of noncollinear AFMs as well as realizing antiferromagnetic spin caloritronics that exhibits promising prospects for energy conversion and information processing.

DOI: 10.1103/PhysRevApplied.18.024007

I. INTRODUCTION

The anomalous Nernst effect (ANE) usually refers to the phenomenon that a transverse electric voltage can be generated by a temperature gradient in magnetic materials, which is perpendicular to both the magnetization and temperature gradient. Conventionally, the ANE is considered proportional to the magnetization and, thus, observed only in ferromagnets [1–5]. Recent studies show that the ANE can also be realized in chiral noncollinear antiferromagnets (AFMs) Mn_3Sn and Mn_3Ge with zero or vanishingly small magnetization due to the topologically nontrivial Berry curvature near the Fermi energy, E_F [6–10]. From a fundamental perspective, the ANE in AFMs is intriguing, since it can be exploited as a sensitive probe for determining key topological parameters of the Weyl physics [7,8]. From a technological perspective, researching the ANE of AFMs is promising to design highly efficient and densely integrated thermopiles, since the lateral configurations of thermoelectric modules enable us to enhance the coverage of the heat source without suffering from the stray fields that cannot be avoided in ferromagnets [7,9].

With abundant magnetic and structural transitions, antiperovskite manganese nitrides, Mn_3AN (where A represents Sn, Ni, Ga, etc., with a perovskite crystal structure but the locations of anion and cation are interchanged), have attracted a revival of attention due to various physical phenomena, such as negative thermal expansion [11,12] and baromagnetic [13], barocaloric [14], and piezomagnetic effects [15–17]. Lately, spin-orbit-torque switching and unconventional spin polarizations have been investigated in these system [18–22], showing tremendous application potential in the field of spintronics. For magnetotransport behavior, the discovery and analysis of the anomalous Hall effect (AHE) in AFM antiperovskites like Mn_3SnN and Mn_3NiN unravel the underlying distinctive physics of these materials [23–25]. Theoretically, the AHE originates from the integration of the Berry curvature for all of the occupied bands, while the ANE is decided by the Berry curvature around E_F. A large AHE thus cannot guarantee a large ANE, and the ANE measurement should be a more sensitive probe for the Berry curvature near E_F than the AHE, which probes the whole Fermi sea [7,8,26–28]. There is theoretical research on the topology analysis of electronic structures of AFM antiperovskites [29], and a large ANE is predicted in the system [30]. However,

*songcheng@mail.tsinghua.edu.cn

the experimental observation of the ANE in this class of materials has not been reported yet. In addition, compared with noncollinear AFM Mn_3X systems (where $X =$ Ge and Sn), the tunable noncollinear magnetic orderings of antiperovskites offer a convenient platform to modulate the ANE by perturbations, such as temperature, doping, and strain [13,23,25,31,32].

Here, we consider antiperovskite AFM Mn_3SnN [the crystal structure is exhibited in Fig. 1(a)], where the AHE is both theoretically and experimentally proved to exist due

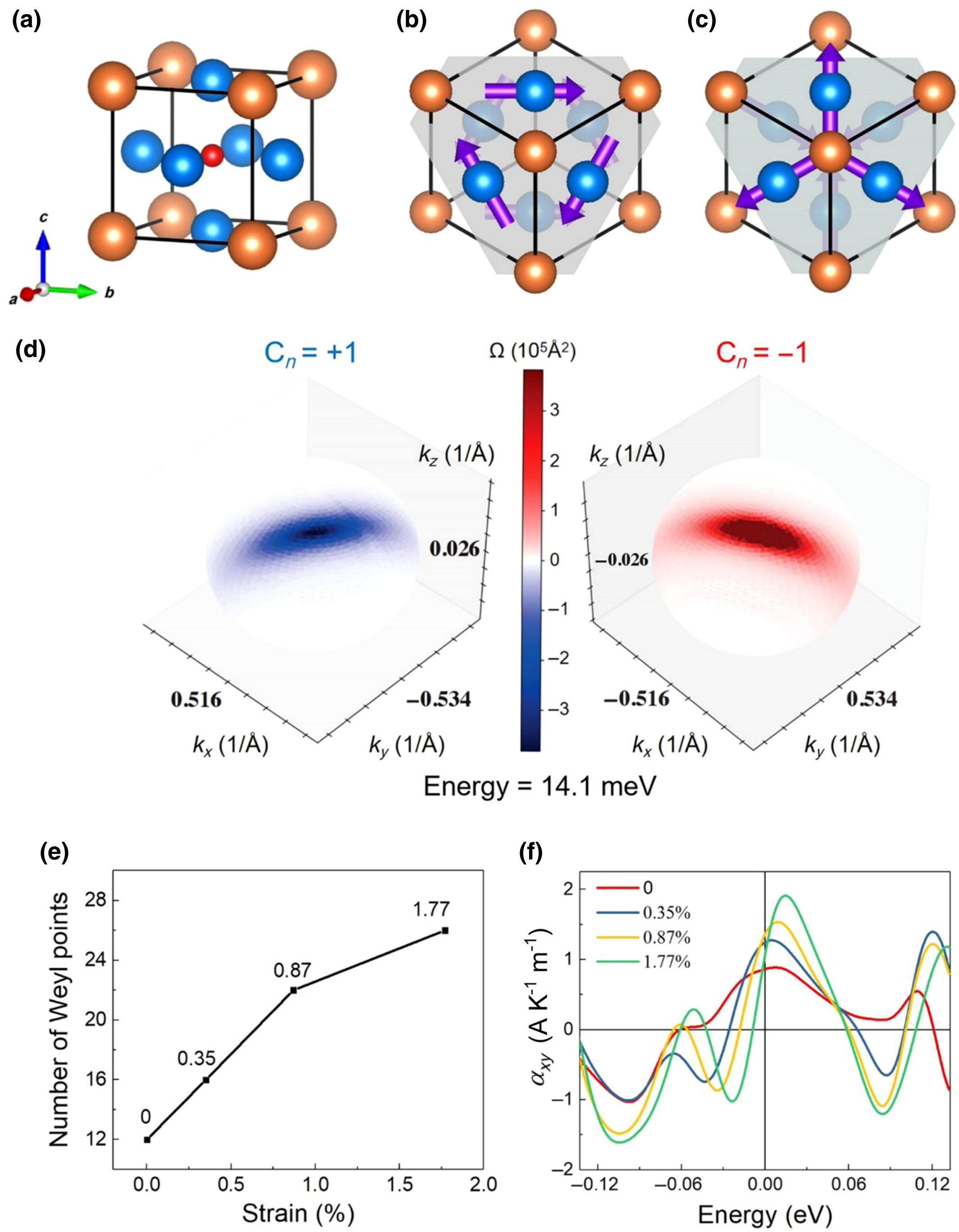

FIG. 1. (a) Crystal structure of Mn_3SnN, where the blue, orange, and red spheres represent Mn, Sn, and N atoms, respectively. Schematics of the magnetic structure of Mn_3SnN (b) Γ_{5g} and (c) Γ_{4g}, where purple arrows denote magnetic moments of Mn atoms and the gray plane donates the Kagome (111) plane. (d) Distribution of the Berry curvature on a closed spherical surface of an inversion pair of Weyl points. (e) Strain dependence of the number of Weyl points with energies between +50 and −50 meV. (f) Energy dependence of the *x*-*y* plane anomalous Nernst conductivity, α_{xy}, with different strain.

to the Berry curvature from the noncollinear AFM structure [23,29,33]. In Mn_3SnN, there are two triangular AFM configurations, Γ_{5g} [Fig. 1(b)] and Γ_{4g} [Fig. 1(c)], where only the Γ_{4g} structure can induce the AHE [23,29,33]. Similarly, from the group-theory analysis of how the spin orders impact on the Berry curvature, the ANE disappears as a result of symmetry in the Γ_{5g} phase [30]. Moreover, since strain can induce the transition of magnetic phases in antiperovskites or influence the magnetic symmetry of the triangular configurations, the Berry curvature and the ANE can be affected accordingly, like the case of the AHE [23,25,30]. Here, we use Mn_3SnN (001) films to research the ANE of AFM antiperovskites. The existence of Weyl points near E_F of Mn_3SnN is responsible for the observed ANE. We also find that the ANE can be effectively manipulated by introducing different biaxial strain. Our research proposes a class of materials to explore the Weyl physics of noncollinear AFMs. The ANE in Mn_3SnN is also promising for realizing antiferromagnetic spin caloritronics [34,35] and has promising prospects for energy conversion and information processing.

II. METHODS

50-nm-thick (001)-oriented Mn_3SnN films are deposited by magnetron sputtering on MgO (001) substrates in an Ar + N_2 mixture using a $Mn_{81}Sn_{19}$ target. Different biaxial strains of 1.77%, 0.87%, 0.35%, and –0.26% are introduced by controlling the N_2-gas partial pressure during the growth of films [23], where the negative value denotes compressive strain and the positive value denotes tensile biaxial strain. Then, an amorphous 50-nm-thick Al_2O_3 insulating layer is deposited at 150 °C by atomic layer deposition. Finally, a 10-nm-thick Pt layer is deposited on the Al_2O_3 insulating layer by magnetron sputtering at room temperature, providing a thermal gradient along the thickness direction of the device as the heater. X-ray diffraction (XRD) and x-ray reflection of the Mn_3SnN films are measured by Cu Kα1 radiation, with λ being 1.5406 Å. The surface roughness is characterized by atomic force microscopy. Magnetic properties are measured using superconducting quantum interference device (SQUID) magnetometry at different temperatures with fields up to 50 kOe. The magnetotransport measurements of the ANE are conducted using a physical-property measurement system. The magnetic field is up to 60 kOe.

The energy band of Mn_3SnN is obtained from first-principles calculations, which are performed in the framework of density-functional theory with the Perdew-Burke-Ernzerhof generalized gradient approximation method. To obtain the most accurate ground-state energy and Fermi level, the tetrahedron method with Blöchl corrections is implemented to sample the Brillouin zone with $18 \times 18 \times 18$ k-meshing size [36,37]. During the calculations, spin-orbit coupling is switched on. A tight-binding model supported by first-principles calculations is obtained by using the Methfessel-Paxton sampling method with $8 \times 8 \times 8$ k-meshing size in the conjunction between the Vienna *ab initio* simulation package and Wannier90 [38, 39]. The entire s, p, and d orbitals of the Mn and Sn atoms are used for building the basis of our tight-binding model. For the N atom, only s and p orbitals are used. We obtain the converged number of Weyl points by increasing the k-meshing size and searching for the local minimum in each grid. Each potential Weyl point is confirmed by calculating its chirality. The chirality of each Weyl point is obtained by calculating the surface integral of the Berry curvature over a small spherical surface enclosing the potential Weyl points [40]. We calculate the anomalous Nernst conductivity based on the anomalous Hall conductivity formula. The anomalous Hall conductivity can be obtained by evaluating the volume integral of the Berry curvature over the entire Brillouin zone with a Fermi-Dirac distribution. In terms of the ANE, we use the Mott relationship to evaluate the anomalous Nernst conductivity based on the intrinsic anomalous Hall conductivity [3].

Thermal simulations are carried out with the finite-element method (FEM) using the COMSOL MULTIPHYSICS software kit. To estimate the temperature difference between the upper and lower surfaces of the Mn_3SnN layer, two-dimensional simulations are carried out on a cross section of the sample. To determine the steady-state temperature distribution of the system with a nonzero current density in the Pt layer, the heat equation $\nabla(\kappa \nabla T) + Q = 0$, is deployed in the FEM simulations, where T is the temperature field to be determined and Q is the Joule heat-source term. In simulations, a Dirichlet boundary condition is given to the bottom surface of the substrate. The temperature of the bottom surface is set to ambient temperature, T_{amb}= 100 K. On the left and right edges of the substrate, periodic boundary conditions are assigned. The rest edges, which stand for surfaces directly exposed to the atmosphere, have a thermally insulating condition, with normal heat-flux density $q_n = 0$. Since all layers are deposited with tight combination, interfacial thermal resistances are omitted for simplicity. The volume heat source in the Pt layer is determined through Joule's law, $Q_{\mathrm{Pt}} = I^2 R / V_{\mathrm{Pt}}$, where V_{Pt} stands for the volume of the Pt layer deposited in experiments [10,41,42].

III. RESULTS AND DISCUSSION

There is a report showing that Mn_3SnN has Weyl points [29]. To study the ANE of Mn_3SnN, we first check the energy band of Mn_3SnN with the magnetic configuration of Γ_{4g} from first-principles calculations (see Fig. S1 within the Supplemental Material) [43]. The tight-binding model supported by first-principles calculations can nicely reproduce the band structure, guaranteeing the accuracy of our calculations. Since the ANE is determined mainly by the

Berry curvature of Weyl points around E_F [7,8,26–28], we attempt to search for Weyl points near E_F of Mn_3SnN. Each potential Weyl point is confirmed by calculating its chirality. Figure 1(d) exhibits an example of the distribution of the Berry curvature on a spherical surface of a pair of Weyl points with the anisotropic property. The energies of the Weyl points are 14.1 meV and the positions are (0.516, −0.534, 0.026) and (−0.516, 0.534, −0.026), respectively. Each Weyl point produces an effective incoming (−) or outgoing (+) effective magnetic flux, which is the source of the nonzero (±1) Chern number. Considering that strain may influence the band structure of Mn_3SnN, we explore the impact of strain on the Weyl points and the ANE. Figure 1(e) shows the strain dependence of the number of Weyl points with energies between +50 and −50 meV. The number of Weyl points shows an increasing trend as the applied strain increases. The energy dependence of the anomalous Nernst conductivity with different strain is exhibited in Fig. 1(f). It is obvious that, when approaching the Fermi level, the anomalous Nernst conductivity, α_{xy}, presents a peak value. More importantly, the peak value increases with applied strain, showing the close relationship between the ANE and strain. These results give us an insight into the correlation between strain and the Weyl property along with the ANE of Mn_3SnN.

Out-of-plane XRD patterns for 50-nm Mn_3SnN thin films grown on MgO substrates with different biaxial strain, ε (1.77%, 0.87%, 0.35%, and −0.26%), are shown in Fig. 2(a). Apart from the diffraction peaks from the MgO substrate, we can see clear diffraction peaks of Mn_3SnN (00l) planes, indicating the quasi-epitaxial growth of the (001)-oriented Mn_3SnN film. Besides, within the sensitivity of XRD measurements, there is no secondary phase. To determine the in-plane orientation and the epitaxial relationship of the Mn_3SnN film, Φ scans are carried out for the Bragg peaks of the Mn_3SnN film and the MgO substrate. Inspection of the Φ scan (see Fig. S2 within the Supplemental Material) [43] shows that the peaks are separated by 90°. The fourfold symmetry for both the film and substrate confirms the crystallographic orientation relationship being MgO(001)[100]//Mn_3SnN(001)[100]. The XRD patterns also exhibit Mn_3SnN (002) peaks with different positions, revealing different c lattice constants of the films. Therefore, different biaxial strains are introduced into the film ascribed to the volume change of the lattice and can be calculated using the formula $(\Delta c/c_0)/\varepsilon = -(2\upsilon/1-\upsilon)$, where $\Delta c/c_0$ represents the relative variation in c-axis length and υ is the Poisson ratio [15–17,23]. The surface morphology of the film measured by atomic force microscopy shows that the whole film is continuous and flat (see Fig. S3 within the Supplemental Material) [43]. The surface roughness R_a is 0.278 nm for the film, with the biaxial strain being 0.87%.

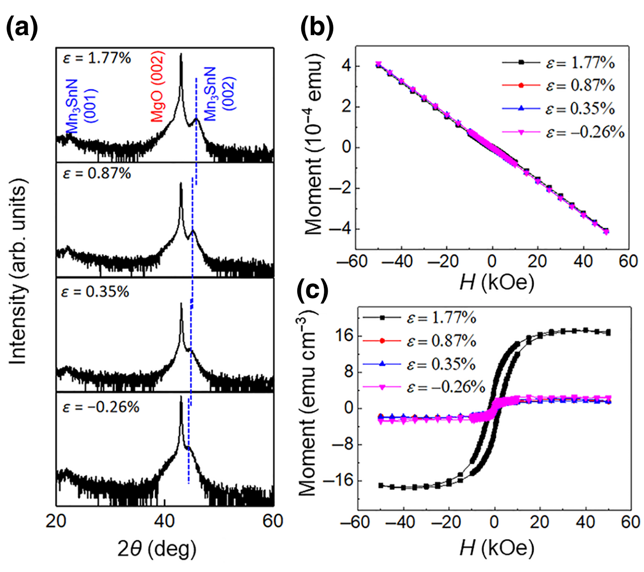

FIG. 2. (a) XRD patterns of (001)-oriented Mn_3SnN films deposited on MgO (001) substrate with different biaxial strain, ε. Magnetization curves of Mn_3SnN (001) films with different biaxial strain, ε, by applying an in-plane magnetic field (b) with and (c) without diamagnetic background from the substrate at 100 K.

The magnetic property of the film is characterized by SQUID, where we apply an in-plane magnetic field, consistent with the measurement configuration for the ANE curves. Figure 2(b) presents four magnetization curves of the (001)-oriented Mn_3SnN films with different biaxial strain at 100 K. At a glance, all curves show diamagnetic behavior due to the diamagnetic background of the MgO substrate, indicating the AFM characteristic of the Mn_3SnN (001) films [44,45]. Corresponding magnetization curves after subtracting the diamagnetic background are presented in Fig. 2(c). Remarkably, the films with biaxial strains of 0.87%, 0.35%, and −0.26% display tiny in-plane uncompensated magnetizations of about 1.81, 2.03, and 2.65 emu cm^{-3}, respectively, and the magnetization of the film with a biaxial strain of 1.77% reaches about 17.3 emu cm^{-3} (the larger magnetization is due to the piezomagnetic effect of Mn_3SnN [15–17,23]). The appearance of uncompensated magnetization may be caused by imperfect growth or the slight spin canting of the film, which is also verified in other noncollinear AFMs [23,24,46–48].

Then, we measure the ANE of the (001)-oriented Mn_3SnN film with different biaxial strains, using the measurement geometry shown in Fig. 3(a) at 100 K. The temperature gradient, ∇T, is applied out of plane along the thickness direction by the Pt heater, and the in-plane thermal gradient generated by the heater can be neglected, since the heating Pt strip exactly covers the whole Mn_3SnN strip (see Fig. S4 in the Supplemental Material) [43]. The applied magnetic field is in plane along the y direction. The anomalous Nernst voltage, V_{ANE}, is thus measured perpendicular to both the temperature gradient and external

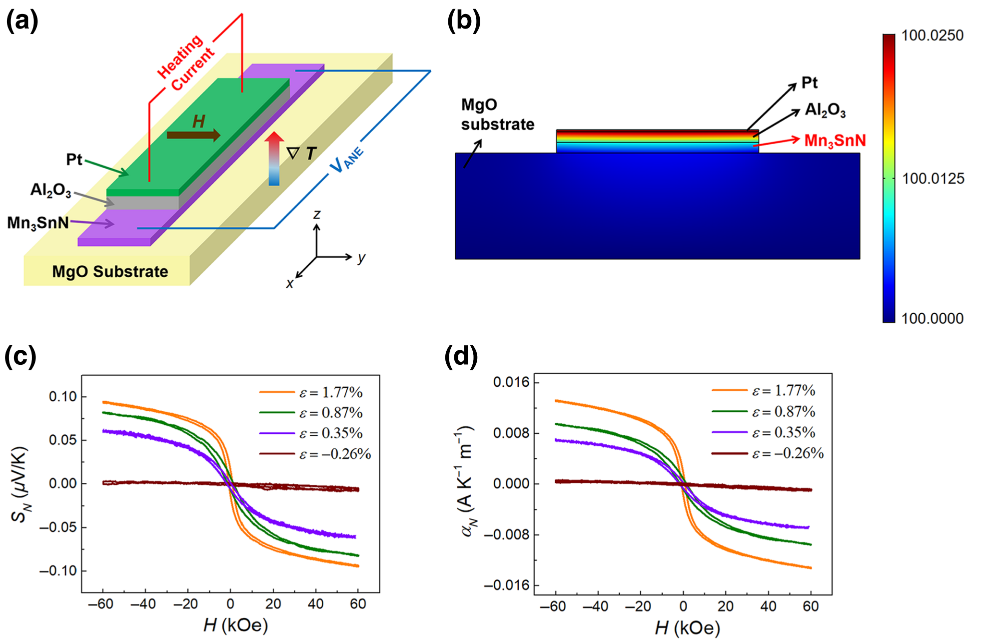

FIG. 3. (a) Schematic of the measurement of the anomalous Nernst effect. Temperature gradient, ∇T, is applied out of plane along the z axis by the Pt heater. Magnetic field is applied in plane along the y axis. Anomalous Nernst voltage, V_{ANE}, is measured along the x axis. (b) Temperature distribution of the schematic model along the z axis (thickness direction) using the finite-element modeling simulation with $I = 15$ mA in the Pt heater. Magnetic field dependence of (c) S_N and (d) α_N for films with different biaxial strain, ε, measured at 100 K. Applied electrical current for heating is 15 mA.

magnetic field. To obtain the anomalous Nernst signal (transverse thermopower), S_N, of Mn_3SnN, we first need to acquire the temperature difference between the top and bottom of the Mn_3SnN film. Since the Joule heat produced by the Pt heater defuses along the thickness direction of the device, and the electrical contact of Mn_3SnN and the Pt heater is separated by the Al_2O_3 insulator, direct detection is difficult. Hence, the temperature difference, ΔT, here is evaluated by simulations. The thermal power density produced by Pt is obtained by measuring the actual resistance of the Pt layer. The geometrical size of the device is $1000 \times 100\ \mu m^2$. The material properties that are needed for the simulation of the temperature distribution are the solid heat capacity at constant pressure, C_p; the solid thermal conductivity, κ; and the solid density. C_p of Mn_3SnN is 75 J $(\mathrm{mol\ K})^{-1}$ [49] and the solid density is 8.47 g cm^{-3}. Since $Mn_{3.1}Zn_{0.5}Sn_{0.4}N$ is also an antiperovskite manganese nitride with a similar crystal structure to that of Mn_3SnN, the solid thermal conductivity of Mn_3SnN is assumed using κ of $Mn_{3.1}Zn_{0.5}Sn_{0.4}N$, which is 11 W/m K [50]. Through the finite-element modeling simulation, the temperature distribution of the schematic model along the thickness direction, with $I = 15$ mA in the Pt heater, is shown in Fig. 3(b). Results of the simulations show that the most significant temperature drop takes place within the Al_2O_3 layer, and the temperature difference, ΔT, for the upper and lower surfaces of the Mn_3SnN layer is calculated to be 6.9×10^{-3} K.

According to the formula

$$S_N = \frac{V_{\mathrm{ANE}}}{\Delta T}\frac{L_z}{L_x}, \tag{1}$$

where L_x and L_z represent the lengths of the Mn_3SnN layer along the x and z (thickness) axes, the magnetic-field-dependent S_N (the applied electrical current for heating is 15 mA) for the (001)-oriented Mn_3SnN film with biaxial strains of −0.26%, 0.35%, 0.87%, and 1.77% is shown in Fig. 3(c). The film with $\varepsilon = -0.26\%$ merely shows a linear relationship between S_N and the magnetic field, revealing that the Γ_{5g} magnetic configuration dominates the magnetic configuration of Mn_3SnN in this case [30]. For the Mn_3SnN film with $\varepsilon = 0.35\%$, S_N reverses sign when the magnetic field is swept between +60 and −60 kOe and the reversal is hysteretic. The observation of a spontaneous zero-field value reveals an obvious ANE in Mn_3SnN, indicating that the magnetic configuration is mainly Γ_{4g} [30]. Considering the tiny magnetization of the film, the obvious ANE signals observed in our experiments mainly originate from the Berry curvature of the Weyl points around the Fermi level, as shown in Fig. 1(d). Besides, as exhibited in Fig. 2(c), the two films above have comparable magnetization, further confirming that the clear hysteresis loop of the ANE signals is not caused by uncompensated magnetization [7–9].

For the Mn_3SnN film with $\varepsilon = 0.87\%$, the ANE is enhanced but the magnetization remains almost unchanged, revealing that strain can improve the ANE through the modulation of Weyl points, as shown in Fig. 1(e). The ANE is further enhanced in the film with larger biaxial strain ($\varepsilon = 1.77\%$), where larger magnetization also appears due to the piezomagnetic effect of Mn_3SnN [15–17,23]. In this case, strain may reduce the magnetic space group of the Γ_{4g} magnetic configuration from $R\bar{3}m'$ to $C'2/m'$ [23,24,29,33] through the canting of the magnetic moments, further enhancing the Berry curvature of Mn_3SnN. The existence of the Γ_{4g} magnetic configuration here is verified by comparing the in-plane and out-of-plane magnetization of the film (see Fig. S5 within the Supplemental Material). The calculated ANE coefficients of the Mn_3SnN film with ε of 0.35%, 0.87%, and 1.77% are 0.058 ± 0.007, 0.083 ± 0.006, and 0.094 ± 0.004 μV/K, respectively. The value of S_N in our Mn_3SnN film is comparable to other noncollinear AFM films like the Mn_3Ge thin film (0.10 μV/K) [9], and is smaller than 0.3 [7] or 0.27 μV/K [10] observed in the Mn_3Sn single crystal. The relatively small value in our experiments is possibly due to the mixing of Γ_{4g} and Γ_{5g} structures along with the imperfect growth of the thin films. Besides, like the AHE [21,22,51], the maximum ANE can be obtained when the magnetic field is applied in the Kagome plane, yet we are unable to access this measurement geometry using our (001)-oriented thin films; thus, the measured value of S_N is inevitably smaller.

To better understand the ANE of Mn_3SnN films with different biaxial strain, we also measure the resistivity, Seebeck coefficient, and AHE of the films (see Table S1 and Fig. S6 within the Supplemental Material) [43] to obtain the anomalous Nernst conductivity, α_N, of the films. According to the ANE formula [7],

$$S_N = \rho(\alpha_N - S\sigma_H), \tag{2}$$

α_N is calculated as

$$\alpha_N = S_N/\rho + S\sigma_H. \tag{3}$$

Here, ρ is the longitudinal resistivity and S is the longitudinal Seebeck coefficient of the films. σ_H is the Hall conductivity, which is calculated by $\sigma_H = -\rho_H/\rho^2$. ρ_H is the transverse Hall resistivity obtained from the AHE of the Mn_3SnN films. Then, we obtain the ANE curve exhibited by the anomalous Nernst conductivity, α_N, as shown in Fig. 3(d). Obviously, for α_N, the strain dependency is the same as that of S_N. The experimental results are also consistent with our theoretical calculations in Fig. 1, providing convincing evidence for the strain dependency of the ANE in Mn_3SnN films.

To further understand the observed ANE signals, we measure the field dependence of V_{ANE} in Mn_3SnN films with different electrical current, *I*. The electrical current applied to the Pt heater is in the range from 1 to 15 mA. As shown in Fig. 4(a), for the film with a biaxial strain of 0.87%, obvious ANE signals can be observed with electrical currents larger than 1 mA, and V_{ANE} increases with the increasing electrical current. Likewise, the same phenomenon can be observed in films with other biaxial strain (see Fig. S7 within the Supplemental Material) [43]. Accordingly, the dependence of V_{ANE} derived from the ANE on I^2 of the above Mn_3SnN films with different biaxial strain is shown in Fig. 4(b). We can observe that V_{ANE} is proportional to I^2, which satisfies the definition of the ANE, since Joule heat, and thus, ∇T, produced by the Pt layer is proportional to I^2. From the slope of the lines, we can conclude that the Mn_3SnN film with $\varepsilon = 1.77\%$ has the largest transverse anomalous Nernst coefficient, further confirming the strain-controlled ANE of Mn_3SnN films. We also measure the ANE of the Mn_3SnN film with $\varepsilon = 1.77\%$ at different temperatures (see Fig. S8 within the Supplemental Material) [43]. As expected, both the magnitude and the hysteresis window of the S_N-H curves

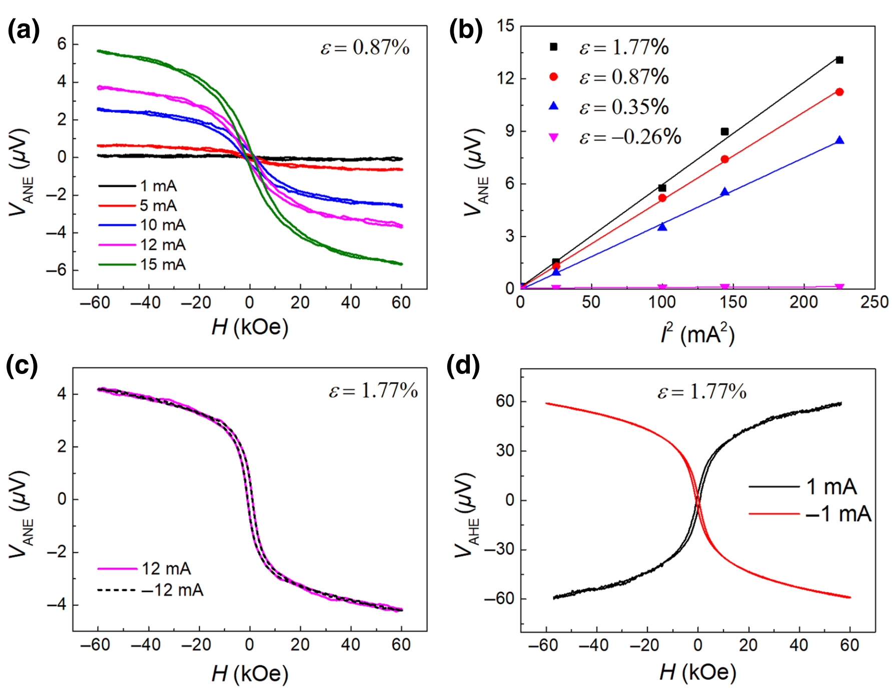

FIG. 4. (a) Field dependence of V_{ANE} in Mn_3SnN film ($\varepsilon = 0.87\%$) with different electrical currents, *I*, at 100 K. (b) Dependence of V_{ANE} on I^2 in the Pt heater in Mn_3SnN films with different biaxial strain. (c) ANE of Mn_3SnN film, with biaxial strain of 1.77%, measured under both positive and negative electrical currents of 12 mA. (d) AHE of the same sample measured with a detection current of ± 1 mA.

increase with decreasing temperature, which confirms that the ANE is related to the noncollinear magnetic structure.

To confirm that the measured voltage signal originates from the ANE, we also use a negative electrical current in the Pt layer, as shown in Fig. 4(c). Evidently, the ANE curves are almost coincident under both positive and negative currents, independent of the current direction in the Pt heater. This phenomenon reveals the typical feature of the ANE because both positive and negative currents in the Pt heater generate ∇T along the same direction. For comparison, we measure the AHE of the film with both positive and negative electrical currents flowing through Mn_3SnN at 100 K (the detection current is 1 mA). Differently, the sign of the anomalous Hall voltage, V_{AHE}, changes with the polarity of the electrical current in the Mn_3SnN film, as shown in Fig. 4(d). Therefore, the hysteresis loop in Fig. 4(a) arises from the ANE rather than other effects.

IV. CONCLUSIONS

We observe obvious ANE signals in the (001)-oriented Mn_3SnN thin films at 100 K, which can be ascribed to the existence of Weyl points near E_F of Mn_3SnN. The ANE can be controlled by biaxial strain in the film, which can change the Weyl property of Mn_3SnN and induce the transformation of noncollinear AFM structures. Moreover, the ANE can be further improved in films with larger biaxial strain, because strain may break the symmetry of the magnetic space group of the Γ_{4g} magnetic configuration through the canting of the magnetic moments due to the piezomagnetic effect of Mn_3SnN; thus, the Berry curvature of Mn_3SnN is influenced accordingly. On one hand, our findings extend the material choice for the ANE in AFMs and provide a class of materials to explore the Weyl physics of noncollinear AFMs. On the other hand, the ANE in Mn_3SnN shows promising prospects for spin caloritronics with extensive applications in energy conversion and information processing.

ACKNOWLEDGMENTS

This work is supported by the Ministry of Science and Technology of China (Grant No. 2021YFA1401500), the National Natural Science Foundation of China (Grants No. 51871130 and No. 12022416), the Natural Science Foundation of Beijing Municipality (Grant No. JQ20010), and the Hong Kong Research Grants Council (Grants No. ECS26302118, No. 16305019, No. 16306220 and No. N_HKUST626/18).

The authors declare no competing interest.

[1] A. W. Smith, The transverse thermomagnetic effect in nickel and cobalt, Phys. Rev. **33**, 295 (1911).

[2] W.-L. Lee, S. Watauchi, V. L. Miller, R. J. Cava, and N. P. Ong, Anomalous Hall Heat Current and Nernst Effect in the $CuCr_2Se_{4-x}Br_x$ Ferromagnet, Phys. Rev. Lett. **93**, 226601 (2004).

[3] D. Xiao, Y. Yao, Z. Fang, and Q. Niu, Berry Phase Effect in Anomalous Thermoelectric Transport, Phys. Rev. Lett. **97**, 026603 (2006).

[4] J. Weischenberg, F. Freimuth, S. Blügel, and Y. Mokrousov, Scattering-independent anomalous Nernst effect in ferromagnets, Phys. Rev. B **87**, 060406(R) (2013).

[5] Z. Shi, S. J. Xu, L. Ma, S. M. Zhou, and G. Y. Guo, Anomalous Nernst Effect in Epitaxial $L1_0FePd1_{-x}Pt_x$ Alloy Films: Berry Curvature and Thermal Spin Current, Phys. Rev. Appl. **13**, 054044 (2020).

[6] X. Li, L. Xu, L. Ding, J. Wang, M. Shen, X. Lu, Z. Zhu, and K. Behnia, Anomalous Nernst and Righi-Leduc Effect in Mn_3Sn: Berry Curvature and Entropy Flow, Phys. Rev. Lett. **119**, 056601 (2017).

[7] M. Ikhlas, T. Tomita, T. Koretsune, M. T. Suzuki, D. NishioHamane, R. Arita, Y. Otani, and S. Nakatsuji, Large anomalous Nernst effect at room temperature in a chiral antiferromagnet, Nat. Phys. **13**, 1085 (2017).

[8] C. Wuttke, F. Caglieris, S. Sykora, F. Scaravaggi, A. U. B. Wolter, K. Manna, V. Süss, C. Shekhar, C. Felser, B. Büchner, and C. Hess, Berry curvature unravelled by the anomalous Nernst effect in Mn_3Ge, Phys. Rev. B **100**, 085111 (2019).

[9] D. Hong, N. Anand, C. Liu, H. Liu, I. Arslan, J. E. Pearson, A. Bhattacharya, and J. S. Jiang, Large anomalous Nernst and inverse spin Hall effects in epitaxial thin films of Mn_3Ge, Phys. Rev. Mater. **4**, 094201 (2020).

[10] H. Narita, M. Ikhlas, M. Kimata, A. A. Nugroho, S. Nakatsuji, and Y. Otani, Anomalous Nernst effect in a microfabricated thermoelectric element made of chiral antiferromagnet Mn_3Sn, Appl. Phys. Lett. **111**, 202404 (2017).

[11] K. Takenaka and H. Takagi, Giant negative thermal expansion in Ge-doped anti-perovskite manganese nitrides, Appl. Phys. Lett. **87**, 261902 (2005).

[12] H. Lu, Y. Sun, S. Deng, K. Shi, L. Wang, W. Zhao, H. Han, S. Deng, and C. Wang, Tunable negative thermal expansion and structural evolution in antiperovskite $Mn_3Ga_{1-x}Ge_xN$ $(0 \leq x \leq 1.0)$, J. Am. Ceram. Soc. **100**, 5739 (2017).

[13] K. Shi, Y. Sun, J. Yan, S. Deng, L. Wang, H. Wu, P. Hu, H. Lu, M. I. Malik, Q. Huang, and C. Wang, Baromagnetic effect in antiperovskite $Mn_3Ga_{0.95}N_{0.94}$ by neutron powder diffraction analysis, Adv. Mater. **28**, 3761 (2016).

[14] D. Matsunami, A. Fujita, K. Takenaka, and M. Kano, Giant barocaloric effect enhanced by the frustration of the antiferromagnetic phase in Mn_3GaN, Nat. Mater. **14**, 73 (2015).

[15] D. Boldrin, A. P. Mihai, B. Zou, J. Zemen, R. Thompson, E. Ware, B. V. Neamtu, L. Ghivelder, B. Esser, D. W. McComb, P. Petrov, and L. F. Cohen, Giant piezomagnetism in Mn_3NiN, ACS Appl. Mater. Interfaces **10**, 18863 (2018).

[16] J. Zemen, Z. Gercsi, and K. G. Sandeman, Piezomagnetism as a counterpart of the magnetovolume effect in magnetically frustrated Mn-based antiperovskite nitrides, Phys. Rev. B **96**, 024451 (2017).

[17] P. Lukashev, R. F. Sabirianov, and K. Belashchenko, Theory of the piezomagnetic effect in Mn-based antiperovskites, Phys. Rev. B **78**, 184414 (2008).

[18] T. Nan, C. X. Quintela, J. Irwin, G. Gurung, D. F. Shao, J. Gibbons, N. Campbell, K. Song, S.-Y. Choi, L. Guo, *et al.*, Controlling spin current polarization through non-collinear antiferromagnetism, Nat. Commun. **11**, 4671 (2020).

[19] G. Gurung, D. F. Shao, and E. Y. Tsymbal, Spin-torque switching of noncollinear antiferromagnetic antiperovskites, Phys. Rev. B **101**, 140405(R) (2020).

[20] T. Hajiri, K. Matsuura, K. Sonoda, E. Tanaka, K. Ueda, and H. Asano, Spin-Orbit-Torque Switching of Noncollinear Antiferromagnetic Antiperovskite Manganese Nitride Mn_3GaN, Phys. Rev. Appl. **16**, 024003 (2021).

[21] Y. You, H. Bai, X. Feng, X. Fan, L. Han, X. Zhou, Y. Zhou, R. Zhang, T. Chen, F. Pan, and C. Song, Cluster magnetic octupole induced out-of-plane spin polarization in antiperovskite antiferromagnet, Nat. Commun. **12**, 6524 (2021).

[22] T. Hajiria, S. Ishino, K. Matsuura, and H. Asano, Electrical current switching of the noncollinear antiferromagnet Mn_3GaN, Appl. Phys. Lett. **115**, 052403 (2019).

[23] Y. You, H. Bai, X. Chen, Y. Zhou, X. Zhou, F. Pan, and C. Song, Room temperature anomalous Hall effect in antiferromagnetic Mn_3SnN films, Appl. Phys. Lett. **117**, 222404 (2020).

[24] D. Boldrin, I. Samathrakis, J. Zemen, A. Mihai, B. Zou, F. Johnson, B. D. Esser, D. W. McComb, P. K. Petrov, H. Zhang, and L. F. Cohen, The anomalous Hall effect in non-collinear antiferromagnetic Mn_3NiN thin films, Phys. Rev. Matter. **3**, 094409 (2019).

[25] D. Boldrin, F. Johnson, R. Thompson, A. P. Mihai, B. Zou, J. Zemen, J. Griffiths, P. Gubeljak, K. L. Ormandy, P. Manuel, D. D. Khalyavin, B. Ouladdiaf, N. Qureshi, P. Petrov, W. Branford, and L. F. Cohen, The biaxial strain dependence of magnetic order in spin frustrated Mn_3NiN thin films, Adv. Funct. Mater. **29**, 1902502 (2019).

[26] A. Sakai, Y. P. Mizuta, A. A. Nugroho, R. Sihombing, T. Koretsune, M. T. Suzuki, N. Takemori, R. Ishii, D. Nishio-Hamane, R. Arita, P. Goswami, and S. Nakatsuji, Giant anomalous Nernst effect and quantum-critical scaling in a ferromagnetic semimetal, Nat. Phys. **14**, 1119 (2018).

[27] Y. Sakuraba, K. Hyodo, A. Sakuma, and S. Mitani, Giant anomalous Nernst effect in the $Co_2MnAl_{1-x}Si_x$ Heusler alloy induced by Fermi level tuning and atomic ordering, Phys. Rev. B **101**, 134407 (2020).

[28] H. Yang, W. You, J. Wang, J. Huang, C. Xi, X. Xu, C. Cao, M. Tian, Z. A. Xu, J. Dai, and Y. Li, Giant anomalous Nernst effect in the magnetic Weyl semimetal $Co_3Sn_2S_2$, Phys. Rev. Mater. **4**, 024202 (2018).

[29] V. T. N. Huyen, M. Suzuki, K. Yamauchi, and T. Oguchi, Topology analysis for anomalous Hall effect in the non-collinear antiferromagnetic states of Mn_3AN (A = Ni, Cu, Zn, Ga, Ge, Pd, In, Sn, Ir, Pt), Phys. Rev. B **100**, 094426 (2019).

[30] X. Zhou, J. P. Hanke, W. Feng, S. Blügel, Y. Mokrousov, and Y. Yao, Giant anomalous Nernst effect in noncollinear antiferromagnetic Mn-based antiperovskite nitrides, Phys. Rev. Mater. **4**, 024408 (2020).

[31] K. Takenaka1, T. Inagaki, and H. Takagi, Conversion of magnetic structure by slight dopants in geometrically frustrated antiperovskite Mn_3GaN, Appl. Phys. Lett. **95**, 132508 (2009).

[32] S. Iikubo, K. Kodama, K. Takenaka, H. Takagi, and S. Shamoto, Magnetovolume effect in $Mn_3Cu_{1-x}Ge_xN$ related to the magnetic structure: Neutron powder diffraction measurements, Phys. Rev. B **77**, 020409 (2008).

[33] G. Gurung, D. F. Shao, T. R. Paudel, and E. Y. Tsymbal, Anomalous Hall conductivity of a non-collinear magnetic antiperovskite, Phys. Rev. Mater. **3**, 044409 (2019).

[34] G. E. W. Bauer, E. Saitoh, and B. J. van Wees, Spin caloritronics, Nat. Mater. **11**, 391 (2012).

[35] S. R. Boona, R. C. Myers, and J. P. Heremans, Spin caloritronics, Energy Environ. Sci. **7**, 885 (2014).

[36] J. P. Perdew, K. Burke, and M. Ernzerhof, Generalized Gradient Approximation Made Simple, Phys. Rev. Lett. **77**, 3865 (1996).

[37] P. E. Blöchl, O. Jepsen, and O. K. Andersen, Improved tetrahedron method for Brillouin-zone integrations, Phys. Rev. B **49**, 16223 (1994).

[38] M. Methfessel and A. T. Paxton, High-precision sampling for Brillouin-zone integration in metals, Phys. Rev. B **40**, 3616 (1989).

[39] A. A. Mostofi, J. R. Yates, Y. S. Lee, I. Souza, D. Vanderbilt, and N. Marzari, Wannier90: A tool for obtaining maximally-localised Wannier functions, Comput. Phys. Commun. **178**, 685 (2008).

[40] D. Gosálbez-Martínez, I. Souza, and D. Vanderbilt, Chiral degeneracies and Fermi-surface Chern numbers in bcc Fe, Phys. Rev. B **92**, 085138 (2015).

[41] A. N. Burgess, K. E. Evans, M. Mackay, and S. J. Abbott, Comparison of transient thermal conduction in tellurium and organic dye based digital optical storage media, J. Appl. Phys. **61**, 74 (1987).

[42] H. Fangohr, D. S. Chernyshenko, M. Franchin, T. Fischbacher, and G. Meier, Joule heating in nanowires, Phys. Rev. B **84**, 054437 (2011).

[43] See the Supplemental Material http://link.aps.org/supplemental/10.1103/PhysRevApplied.18.024007 for the energy band, Φ scan patterns, surface morphology, magnetization, optical image for the ANE measurement, and AHE data of Mn_3SnN films.

[44] X. Chen, S. Shi, G. Shi, X. Fan, C. Song, X. Zhou, H. Bai, L. Liao, Y. Zhou, H. Zhang, A. Li, *et al.*, Observation of the antiferromagnetic spin Hall effect, Nat. Mater. **20**, 800 (2021).

[45] H. Bai, L. Han, X. Y. Feng, Y. J. Zhou, R. X. Su, Q. Wang, L. Y. Liao, W. X. Zhu, X. Z. Chen, F. Pan, X. L. Fan, and C. Song, Observation of the Spin Splitting Torque in a Collinear Antiferromagnet RuO_2, Phys. Rev. Lett. **128**, 197202 (2022).

[46] Y. You, X. Chen, X. Zhou, Y. Gu, R. Zhang, F. Pan, and C. Song, Anomalous Hall effect-like behavior with in-plane magnetic field in noncollinear antiferromagnetic Mn_3Sn films, Adv. Electron. Mater. **5**, 1800818 (2019).

[47] F. Hu, G. Xu, Y. You, Z. Zhang, Z. Xu, Y. Gong, E. Liu, H. Zhang, E. Liu, W. Wang, and F. Xu, Tunable magnetic and transport properties of Mn_3Ga thin films on Ta/Ru seed layer, J. Appl. Phys. **123**, 103902 (2018).

[48] A. Markou, J. M. Taylor, A. Kalache, P. Werner, S. S. P. Parkin, and C. Felser, Noncollinear antiferromagnetic Mn_3Sn films, Phys. Rev. Mater. **2**, 051001 (2018).

[49] Y. Sun, Y. Guo, Y. Tsujimoto, C. Wang, J. Li, X. Wang, H. L. Feng, C. I. Sathish, Y. Matsushita, and K. Yamaura, Unusual magnetic hysteresis and the weakened transition behavior induced by Sn substitution in Mn_3SbN, J. Appl. Phys. **115**, 043509 (2014).

[50] H. Cao, Y. Su, D. Zhang, and Q. Ouyang, Fabrication, mechanical and thermal behaviors of antiperovskite manganese nitride $Mn_{3.1}Zn_{0.5}Sn_{0.4}N$ reinforced aluminum matrix composites, Composites, Part B **223**, 109080 (2021).

[51] S. Nakatsuji, N. Kiyohara, and T. Higo, Large anomalous Hall effect in a non-collinear antiferromagnet at room temperature, Nature **527**, 212 (2015).